Decision Making: Applications in Management and Engineering

ISSN: 2560-6018, eISSN: 2620-0104

COMPARATIVE EVALUATION OF COPPER (II) OXIDE AND ZINC OXIDE NANOPARTICLES FOR DIABETIC WOUND HEALING APPLICATIONS

Subhasri Bogadi[1], Veera Venkata Satyanarayana Reddy Karri[1]*, Gowthamarajan Kuppusamy[1], Vetriselvan Subramaniyan[2]

[1]Department of Pharmaceutics, JSS College of Pharmacy, JSS Academy of Higher Education & Research, Ooty, Tamil Nadu-643001, India. Email ID: subhasriphd@jssuni.edu.in, gowthamsang@jssuni.edu.in

[2]Pharmacology Unit, Jeffrey Cheah School of Medicine and Health Sciences, Monash University, Jalan Lagoon Selatan, Bandar Sunway, 47500 Selangor Darul Ehsan, Malaysia. Email ID: vetricology@gmail.com

[1*]Department of Pharmaceutics, JSS College of Pharmacy, JSS Academy of Higher Education & Research, Ooty, Tamil Nadu-643001, India. Corresponding Author Email ID: ksnreddy87@gmail.com

Abstract

Diabetic wounds, present significant challenges due to their slow healing and high infection risk. This study investigates the therapeutic potential of Copper (II) Oxide (CuO) and Zinc Oxide (ZnO) nanoparticles in enhancing diabetic wound healing. We characterized the physicochemical properties of CuO and ZnO nanoparticles using Dynamic Light Scattering (DLS), scanning electron microscopy (SEM), X-ray diffraction (XRD), and Thermogravimetric Analysis (TGA). In addition to these characterizations, we conducted a series of in vitro studies, including cytotoxicity assays, cell proliferation, and migration assays, antioxidant studies through DPPH and Reactive Oxygen Species (ROS) scavenging assays, and angiogenesis evaluations using the chick chorioallantoic membrane (CAM) assay. These studies revealed a solid potential for mitigating oxidative stress and promoting cellular activities crucial for wound repair. The antibacterial efficacy was assessed by measuring the zone of inhibition, demonstrating effective control over *E. coli* and *S. aureus*. Anti-inflammatory effects were examined by analyzing levels of inflammatory markers such as TNF-Alpha and

interleukins (IL-10), indicating reduced chronic inflammation. The wound healing potential was specifically assessed using NIH 3T3 cell lines in scratch wound healing assays to ensure consistent cell migration and proliferation evaluation. Our results showed that both CuO and ZnO nanoparticles significantly enhance the rate of wound closure. The results suggest that CuO and ZnO nanoparticles significantly benefit diabetic wound healing by promoting cellular activities and controlling infection and inflammation. Further optimization of formulation is needed to enhance efficacy and patient comfort. This study highlights the potential of these nanoparticles in advancing therapeutic approaches for diabetic wounds.

Introduction

Diabetic wounds, particularly diabetic foot ulcers, represent a severe and prevalent complication of diabetes mellitus (1). These wounds are characterized by a prolonged healing process, high susceptibility to infections, and an increased risk of severe outcomes such as amputation (2). The impaired healing observed in diabetic patients is attributed to a combination of factors, including poor blood circulation, neuropathy, immune dysfunction, and chronic inflammation. Hyperglycemia in diabetes leads to the formation of advanced glycation end-products (AGEs), which further disrupt normal wound healing processes (3). The pathophysiology of diabetic wound healing involves a prolonged inflammation phase with elevated levels of inflammatory cytokines like TNF-Alpha and interleukins, which delays the transition to the proliferative phase (4). During the proliferation phase, angiogenesis, fibroblast proliferation, and collagen synthesis are impaired, with the hyperglycemic environment affecting cellular functions and reducing growth factor production. The remodeling phase is also compromised, resulting in fragile and improperly formed scar tissue due to an imbalance between matrix metalloproteinases (MMPs) and their inhibitors (5).

Current treatment strategies for diabetic wounds include debridement, infection control, pressure offloading, and specialized dressings that maintain a moist environment. Advanced therapies such as growth factors, skin substitutes, and hyperbaric oxygen therapy are also employed, though they often come with limitations like high costs, variable efficacy, and limited availability (6). The multifactorial nature of diabetic wound healing necessitates novel therapeutic approaches that can address multiple aspects of the wound healing process simultaneously (7-8). Ideal new strategies should target pathological processes, including oxidative stress, chronic inflammation, impaired angiogenesis, and reduced cell proliferation (9). In this context, metal oxide nanoparticles such as CuO and ZnO emerge as promising candidates for enhancing diabetic wound healing (10). These nanoparticles possess unique properties that can potentially address the limitations of current therapies. CuO and ZnO nanoparticles exhibit significant antioxidant activity, which helps mitigate oxidative stress in the wound environment (11). They also demonstrate antimicrobial solid properties, reducing the risk of wound infections. Furthermore, these nanoparticles can modulate the inflammatory response, promote angiogenesis, and stimulate cell proliferation and migration (12). By targeting multiple facets of the wound healing process, CuO and ZnO nanoparticles offer a comprehensive approach to improving diabetic wound care and addressing the unmet needs in this challenging area of treatment (13-15).

This study's primary objective is to comprehensively evaluate CuO and ZnO nanoparticles' potential in diabetic wound healing applications (16). Specifically, the study aims to characterize the physicochemical properties of these nanoparticles, including their particle size, zeta potential, surface morphology, and crystallinity, using techniques such as SEM and X-ray diffraction (XRD) (17). Another key objective is to assess the antioxidant activity of CuO and ZnO nanoparticles through DPPH and ROS scavenging assays to understand their capacity to counteract oxidative stress, a significant factor in diabetic wounds (18). The study also seeks to evaluate the antibacterial properties of the nanoparticles by measuring the zone of inhibition against common wound pathogens, thereby determining their effectiveness in preventing and controlling infections. Additionally, the impact of CuO and ZnO nanoparticles on inflammatory responses will be investigated through ELISA assays for inflammatory markers such as TNF-Alpha and interleukins (IL-1β, IL-6, IL-10), aiming to elucidate their potential in modulating chronic inflammation associated with diabetic wounds (19-22). Finally, the study will explore the ability of these nanoparticles to promote angiogenesis and enhance cellular activities such as proliferation and migration through assays like tube formation and scratch wound healing.

Hypothesis

Diabetic wounds often present significant challenges to effective healing due to several underlying factors, including persistent chronic inflammation, heightened oxidative stress, increased susceptibility to infections, impaired cellular functions, and insufficient angiogenesis. Chronic inflammation can lead to prolonged tissue damage, impeding the healing process. Elevated ROS levels exacerbate oxidative stress, contributing to cellular damage and delayed wound repair. The increased risk of bacterial infections complicates healing further, while impaired cellular proliferation and migration hinder wound closure. Insufficient angiogenesis restricts the delivery of essential nutrients and oxygen to the damaged tissue, limiting the repair process.

This study hypothesizes that CuO and ZnO nanoparticles, when incorporated into appropriate dosage forms, can significantly address these challenges and enhance diabetic wound healing. It is anticipated that CuO and ZnO nanoparticles will exhibit distinct physicochemical properties, such as varying particle sizes and surface morphologies, influencing their interactions within the wound environment. CuO nanoparticles are expected to display unique characteristics compared to ZnO nanoparticles, potentially affecting their therapeutic efficacy. Both types of nanoparticles are hypothesized to offer substantial antioxidant activity, with CuO nanoparticles likely to exhibit superior ROS scavenging capabilities. By incorporating these nanoparticles into optimized dosage forms, the study expects to enhance their ability to counteract oxidative stress, thereby promoting more effective wound healing. Furthermore, the antibacterial properties of CuO and ZnO nanoparticles are expected to be robust against common wound pathogens, with CuO nanoparticles potentially providing a broader spectrum of antibacterial activity. The effectiveness of these nanoparticles in preventing and controlling infections is anticipated to be significantly improved when delivered through suitable formulations. Regarding anti-inflammatory effects, ZnO nanoparticles are hypothesized to more effectively

modulate inflammatory responses than CuO nanoparticles, as evidenced by reduced cytokine levels. Proper dosage forms are expected to enhance the ability of ZnO nanoparticles to manage chronic inflammation, thereby supporting the overall healing process. Additionally, both CuO and ZnO nanoparticles are anticipated to promote angiogenesis and support cellular proliferation and migration. ZnO nanoparticles are particularly expected to demonstrate greater effectiveness in enhancing vascularization and wound closure. When incorporated into appropriate dosage forms, these nanoparticles are predicted to improve cellular and vascular functions substantially, leading to better wound healing outcomes.

Importantly, while metal oxide nanoparticles are known for their therapeutic potential, their direct application to wound sites can cause adverse effects such as itching or discomfort. Therefore, incorporating these nanoparticles into well-designed dosage forms is crucial to maximizing their therapeutic benefits while minimizing any negative side effects. Such formulations can ensure controlled and sustained release of the nanoparticles, providing a more comfortable and effective treatment for diabetic wounds. In summary, this study posits that CuO and ZnO nanoparticles, when formulated into effective dosage forms, have the potential to address the critical challenges of diabetic wound healing. Their combined antioxidant, antibacterial, and anti-inflammatory properties and ability to support cellular and vascular functions are expected to provide a comprehensive therapeutic approach to enhance wound repair in diabetic conditions.

Materials & methods

2.1 Materials

CuO nanoparticles (purity ≥ 99.5%, particle size < 50 nm) and ZnO nanoparticles (purity ≥ 99.5%, particle size < 30 nm) were procured from Sigma-Aldrich. NIH 3T3 cell lines were cultured in Dulbecco's Modified Eagle Medium (DMEM, high glucose, without phenol red, Cat No. 11965-092) supplemented with 10% Fetal Bovine Serum (FBS, Cat No. 16140-071), both from Thermo Fisher Scientific. Antioxidant activity was evaluated using DPPH (Sigma-Aldrich, Cat No. D9132) and ROS detection kits from Invitrogen (Product No. D6883). Antibacterial assays utilized Nutrient Broth (BD Biosciences, Cat No. 214830) and Mueller-Hinton Agar (BD Biosciences, Cat No. 70192), with Escherichia coli (ATCC 25922) and Staphylococcus aureus (ATCC 25923) as the test strains. Anti-inflammatory effects were measured using ELISA kits for TNF-Alpha and interleukins (IL-1β, IL-6, IL-10) from R&D Systems (Product Nos. DY210, DY206, DY306, DY317). Angiogenesis and cellular proliferation were assessed using tube formation assays (Chemicon, Product No. ECM590) and scratch wound healing assays. Physicochemical characterization was conducted using SEM (EOL JSM-IT200), X-ray Diffraction (XRD, Bruker D8 Advance), and Fourier-transform Infrared Spectroscopy (FTIR, PerkinElmer Spectrum Two). Statistical analyses were performed with GraphPad Prism (Version 9.0).

2.2 Methods

Characterization of nanoparticles

DLS

DLS was used to determine CuO and ZnO nanoparticles' particle size and zeta potential. Given their insolubility in water, nanoparticles were suspended in Dimethyl Sulfoxide (DMSO) at a concentration of 1 mg/mL (23). To ensure proper dispersion, the suspensions were sonicated for 15 minutes. For particle size analysis, 1 mL of the nanoparticle suspension was placed into disposable polystyrene cuvettes. The Zetasizer Nano ZS (Malvern Instruments) analyzed the samples at 25°C, measuring the intensity of scattered light to determine the hydrodynamic diameter and providing an average particle size distribution (24). For zeta potential measurements, 0.8 mL of the suspension was transferred into folded capillary cells. The Zetasizer Nano ZS applied an electric field to measure the electrophoretic mobility, and the zeta potential was calculated using the Smoluchowski equation (25). All measurements were performed in triplicate to ensure accuracy, and results were analyzed using Malvern's Zetasizer software, which provided average values and standard deviations.

2.2.3 Morphology

CuO and ZnO nanoparticles were placed on silicon wafers or carbon-coated copper grids and allowed to air dry (26). The samples were then sputter-coated with gold for 60 seconds using an Emitech K575X sputter coater to prevent charging effects during imaging. The coated samples were then analyzed with a JEOL JSM-IT200 SEM at 15 kV. High-resolution images were captured to evaluate surface morphology and particle size distribution (27). Particle sizes were measured using ImageJ software, with average sizes calculated from multiple photos.

2.2.4 TGA

It was employed to assess the thermal stability and composition of CuO and ZnO nanoparticles. For TGA, approximately 5-10 mg of each nanoparticle sample was accurately weighed and placed into an alumina sample pan (28). The analysis was conducted using a thermogravimetric analyzer (e.g., TA Instruments Q50). The samples were heated from 30°C to 800°C at a constant rate of 10°C/min under a nitrogen atmosphere to prevent oxidation and degradation. The weight loss of the samples was recorded as a function of temperature, and the resulting data were used to evaluate thermal stability, decomposition temperatures, and potential residual content. The TGA curves were analyzed to determine vital thermal properties and confirm the nanoparticles' purity and composition (29).

2.2.5 Powder X-ray Diffraction (XRD)

XRD was employed to analyze the crystalline structure of CuO and ZnO nanoparticles. For powder XRD analysis, a small amount of each nanoparticle powder was loaded into a sample holder, ensuring

even distribution and minimal packing (30). The XRD patterns were recorded using an X-ray diffractometer (PANalytical X'Pert Pro) with a Cu Kα radiation source (wavelength = 1.5406 Å). The diffraction scans were performed over a 2θ range of 10° to 80°, with a scan rate of 2°/min (31). The resulting diffraction patterns were analyzed to identify crystalline phases, determine lattice parameters, and assess phase purity.

2.3 Antioxidant study

2.3.1 DPPH Radical Scavenging Activity

The DPPH radical scavenging assay was conducted to evaluate the antioxidant activity of CuO and ZnO nanoparticles (32). A 0.1 mM DPPH solution was prepared in methanol and kept in the dark to maintain stability. For the assay, 1 mL of each nanoparticle sample, at varying concentrations (10, 20, 30, and 40 µg/mL), was mixed with 2 mL of the DPPH solution (33). The mixture was incubated in the dark at room temperature for 30 minutes. The absorbance of the solution was measured at 517 nm using a spectrophotometer (34). The antioxidant activity was calculated as the percentage inhibition of the DPPH radical using the formula

$$Percentage\ Inhibition = \frac{\text{A control} - A\ sample}{\text{A control}} * 100$$

A control is the absorbance of the DPPH solution without the sample, and a sample is the absorbance with the sample. The assay was performed in triplicate, and the average percentage inhibition was reported as an indicator of the nanoparticles' antioxidant capacity.

2.3.2 ROS Scavenging Activity

The ROS of CuO and ZnO nanoparticles was assessed using a fluorescence-based assay. Specifically, the assay utilized 2,7-dichlorofluorescein diacetate (DCFH-DA), a fluorescent probe that reacts with ROS to produce a green fluorescent signal. For the assay, 1 mL of a 20 µM DCFH-DA solution was prepared in phosphate-buffered saline (PBS). A 1 mL aliquot of each nanoparticle sample, at varying concentrations (10, 20, 30, and 40 µg/mL), was mixed with 1 mL of the DCFH-DA solution (35). The mixture was incubated for 30 minutes at 37°C in the dark to allow the nanoparticles to interact with ROS. Following incubation, 1 mL of hydrogen peroxide (H_2O_2) solution (final concentration 100 µM) was added to the reaction mixture to induce ROS generation (36). The mixture was further incubated for 30 minutes. The absorbance of the solution was measured at 535 nm using a spectrophotometer. The ROS scavenging activity was calculated as the percentage decrease in absorbance intensity compared to the control (sample without nanoparticles) using the formula (37):

$$Percentage\ Scavenging = \frac{\text{Acontrol} - A\ sample}{\text{A control}} * 100$$

A control is the absorbance intensity of the control sample without nanoparticles; a sample is the absorbance intensity with nanoparticles. The assay was performed in triplicate, and the average percentage scavenging was reported as an indicator of the nanoparticles' ROS scavenging capacity.

2.4 Cytotoxicity assay

2.4.1 Cell culture

NIH 3T3 cells were cultured in DMEM supplemented with FBS and 1% penicillin-streptomycin. The cells were incubated at 37°C in a humidified atmosphere with 5% CO_2. For assays, cells were seeded in a 96-well plate at a density of 1 × 10^4 cells per well in 100 µL of DMEM. After planting, the cells could adhere and grow for 24 hours to reach the desired confluence before treatment or assay procedures (38).

2.4.2 Cytotoxicity Assay

Following cell adherence, NIH 3T3 cells were exposed to CuO and ZnO nanoparticles at 10, 20, 30, and 40 µg/mL concentrations. The treatment was carried out for 24, 48, and 72 hours. For assessment, 10 µL of a 5 mg/mL MTT solution was added to each well, and the plates were incubated at 37°C for 4 hours. MTT is reduced by metabolically active cells to form formazan crystals (39). After incubation, the medium was removed, and 100 µL of DMSO was added to dissolve the formazan crystals. Absorbance was measured at 570 nm. The cell viability percentage was calculated relative to the untreated control to determine the cytotoxicity of the test substances using a formula.

$$Cell\ viability\ (\%) = \frac{\text{Average absorbance of sample}}{\text{Average absorbance of control}} * 100$$

2.4.3 Cell Proliferation Assay

For the cell proliferation assay, NIH 3T3 cells were similarly treated with the CuO and ZnO nanoparticles at 10, 20, 30, and 40 µg/mL concentrations. After the same treatment periods of 24, 48, and 72 hours, 10 µL of a 5 mg/mL MTT solution was added to each well and incubated for 4 hours at 37°C (40). Post-incubation, the medium was discarded, and 100 µL of DMSO was added to solubilize the formazan crystals. Absorbance was recorded at 570 nm with a microplate reader (41). The cell proliferation percentage was calculated relative to the untreated control, reflecting the growth and replication of cells under treatment conditions.

2.5 Scratch assay

NIH 3T3 cells were seeded into a 6-well plate at a density of 1 × 10^5 cells per well and allowed to reach confluence over 24 hours. Once the cells reached confluence, a sterile 200 µL pipette tip was used to create a wound in the cell monolayer (42). After wounding, the wells were washed with PBS to remove detached cells. Fresh DMEM containing CuO and ZnO nanoparticles at 10, 20, 30, and 40 µg/mL concentrations was added to the wells. Fresh DMEM without nanoparticles was used to control the wells. The cells were then incubated for 24, 48, and 72 hours to allow for migration into the wound area (43). Images of the wound area were captured at each time point using an inverted microscope. To quantify migration, the wound area was measured using image analysis software, and the percentage of wound closure was calculated using the formula (44-45):

$$Percentage\ Scavenging = \frac{\text{Initial wound area} - woun\quad area\ at\ time\ point}{\text{Initial wound area}} * 100$$

This formula helps to determine the extent to which the CuO and ZnO nanoparticles influence cell migration compared to the control.

2.6 Antibacterial activity

2.6.1 Agar plate method

To evaluate the antibacterial activity of CuO and ZnO nanoparticles, suspensions were prepared in DMSO at 10, 20, 30, and 40 µg/mL concentrations. *E. coli* and *S. aureus* strains were grown overnight in nutrient broth at 37°C with shaking (46). The nutrient broth medium was prepared by dissolving 13 g of nutrient broth powder in 1 L of distilled water, followed by autoclaving at 121°C for 15 minutes to ensure sterility. The bacterial suspensions were adjusted to match a 0.5 McFarland standard for uniform inoculation (47). Mueller-Hinton agar plates were prepared and allowed to solidify. The bacterial suspensions were evenly spread over the agar plates using a sterile swab to create a uniform bacterial lawn. The nanoparticle suspensions were directly applied onto the inoculated agar plates in specified concentrations. The plates were incubated at 37°C for 24 hours. After incubation, the diameters of the clear zones indicating antibacterial activity were measured using a caliper (48). These measurements were recorded for each concentration of CuO and ZnO nanoparticles and each bacterial strain. The effectiveness of the nanoparticles was assessed based on the size of the inhibition zones.

2.7 In-vitro drug release

To evaluate the in vitro drug release of CuO and ZnO nanoparticles, we prepared the nanoparticles at concentrations of 10, 20, 30, and 40 µg/mL. The nanoparticles were suspended in PBS at pH 7.4 to create solutions of each concentration (50). These nanoparticle suspensions were placed into dialysis tubes to separate the nanoparticles from the release medium. The containers were immersed in 50 mL

of fresh PBS at pH 7.4, maintaining a controlled temperature of 37°C to simulate physiological conditions. At specific time points (e.g., 1, 2, 4, 6, 8, 12, 24, 48, and 72 hours), we withdrew 1 mL of the release medium and replaced it with an equal volume of fresh PBS to maintain sink conditions (51). The withdrawn samples were analyzed using UV-Vis spectroscopy to quantify the amount of CuO and ZnO nanoparticles released. We plotted the cumulative release data against time for each concentration (10, 20, 30, and 40 µg/mL) to construct release profiles. The release data were then fitted to various kinetic models (e.g., zero-order, first-order, Higuchi, or Hixson-Crowell) to interpret the release behavior of the nanoparticles (52).

2.8 Reduction in chronic inflammation

To assess the inflammatory response modulation, nanoparticle suspensions of plain CuO and ZnO were prepared at concentrations of 10, 20, 30, and 40 µg/mL using DMSO. After thorough mixing, NIH 3T3 cell lines were treated with these nanoparticle suspensions for 24 or 48 hours. The cell supernatants were then collected for analysis (53). The ELISA for TNF-α and IL-10 was conducted using kits from Koma Biotech Inc., Seoul, Korea, following the manufacturer's protocol. A 96-well plate was coated with capture antibodies specific for TNF-α and IL-10 and incubated overnight at 4°C. The wells were blocked with a blocking buffer at room temperature for 1 hour to prevent non-specific binding. After blocking, standard solutions were added to create a standard curve, followed by the collected cell supernatants (54). The plate was incubated for 2 hours at room temperature or 37°C with gentle shaking. After incubation, the plate was washed 3-5 times with wash buffer to remove unbound substances. Detection antibodies specific to TNF-α and IL-10 were added, and the plate was incubated. Following another round of washes, the substrate solution was added and incubated until color developed (55). Finally, the stop solution was added, and absorbance was measured using a multi-mode plate reader (Tecan M200, Austria) at 450 nm for TNF-α and 450 nm or 490 nm for IL-10. The absorbance readings of the samples were compared to the standard curve to determine the concentrations of TNF-α and IL-10.

2.9 Angiogenesis assay

Fertilized chicken eggs were incubated at 37.5°C with 50-60% humidity. On embryonic day 3, a small hole was made at the broad end for air exchange (56). On day 7 or 8, a 1-2 cm window was created in the shell to expose the CAM, which was then sealed with sterile parafilm. CuO and ZnO nanoparticles were suspended at 10, 20, 30, and 40 µg/mL in sterile PBS, soaked into Whatman filter paper disks, and dried. On day 10, these disks were placed on the CAM near the main blood vessels, with PBS-soaked disks as controls. The windows were resealed, and the eggs were incubated for another 48-72 hours. The CAM was observed, and images were captured for analysis (57-58). Blood vessel formation and vascular density changes were quantified by counting branch points and measuring vessel length and area. Results from treated samples were compared with controls to determine the nanoparticles' effects on angiogenesis.

Results and Discussion

3.1 Characterization

3.1.1 Morphology

SEM analysis revealed that CuO nanoparticles predominantly exhibited a spherical morphology with smooth surfaces and a uniform size distribution (Figure 1 (a)). In contrast, ZnO nanoparticles displayed a mix of spherical and rod-like shapes with more irregular surfaces and some aggregation (Figure 1(b)). These observations confirm the consistent size and shape characteristics of CuO nanoparticles and highlight the variability in morphology for ZnO nanoparticles.

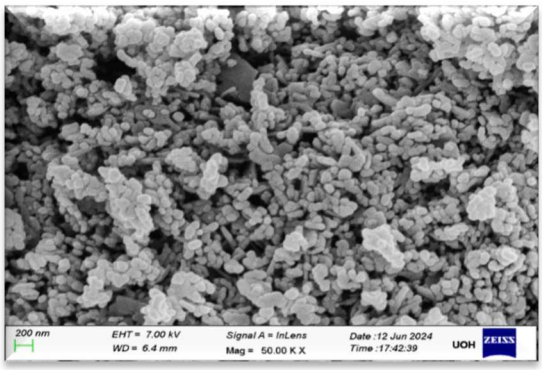

Figure 1 (a): SEM images of CuO nanoparticles

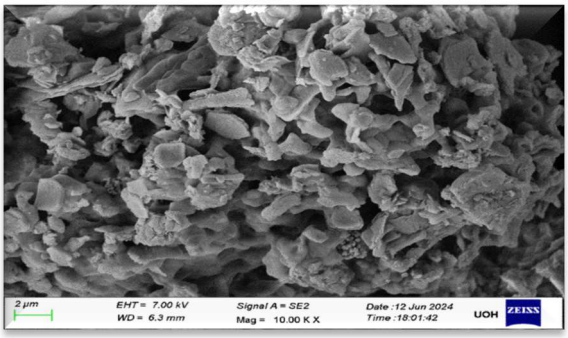

Figure 1 (b): SEM images of ZnO nanoparticles

3.1.2 DLS

The DLS analysis revealed that the average particle size of CuO nanoparticles was 68.11 nm (Figure 1(c)). The PDI for CuO nanoparticles was approximately 0.165, indicating a relatively uniform particle size distribution. The average particle size of ZnO nanoparticles was 74.48 nm (Figure 1 (d)), with a

PDI of approximately 0.188, reflecting a slightly broader size distribution than CuO. The zeta potential measurements showed that CuO nanoparticles had a surface charge of -21.3 mV (Figure 1 (e)), while ZnO nanoparticles had a surface charge of -20.8 mV (Figure 1 (f)).

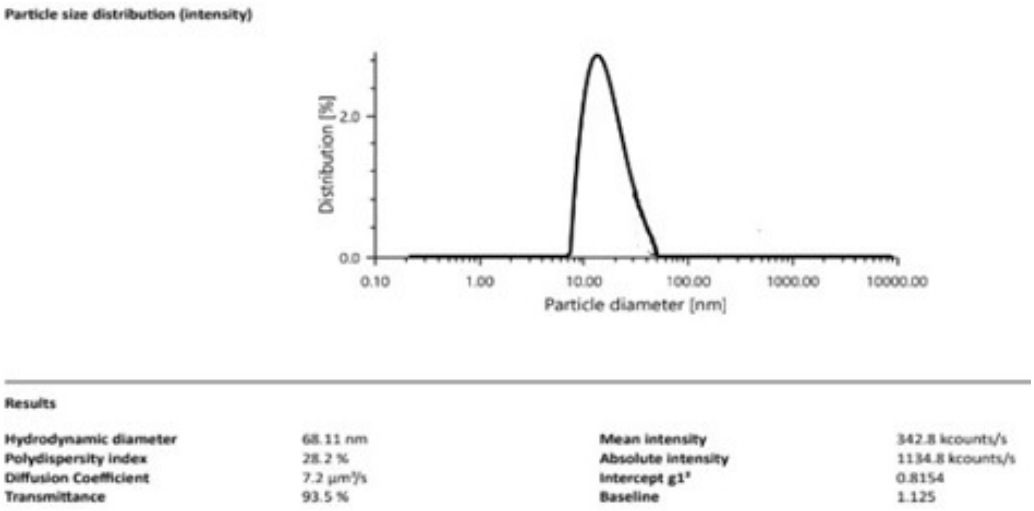

Figure 1 (c): Particle size distribution of CuO nanoparticles

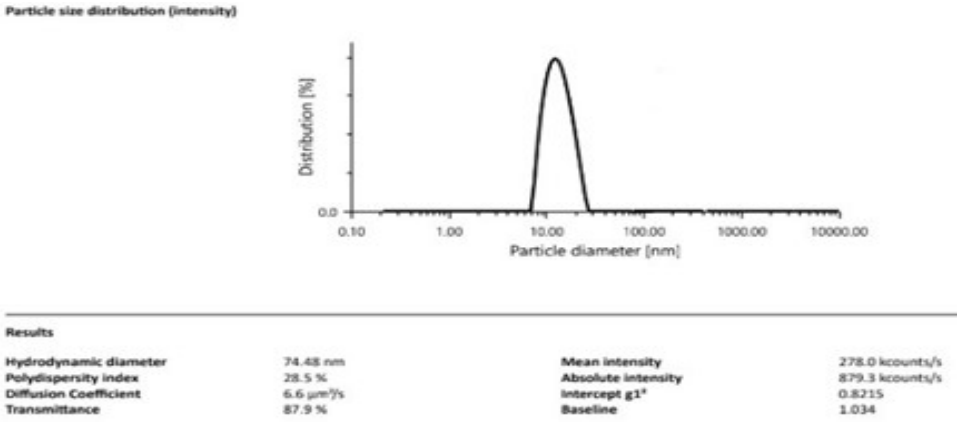

Figure 1 (d): Particle size distribution of ZnO nanoparticles

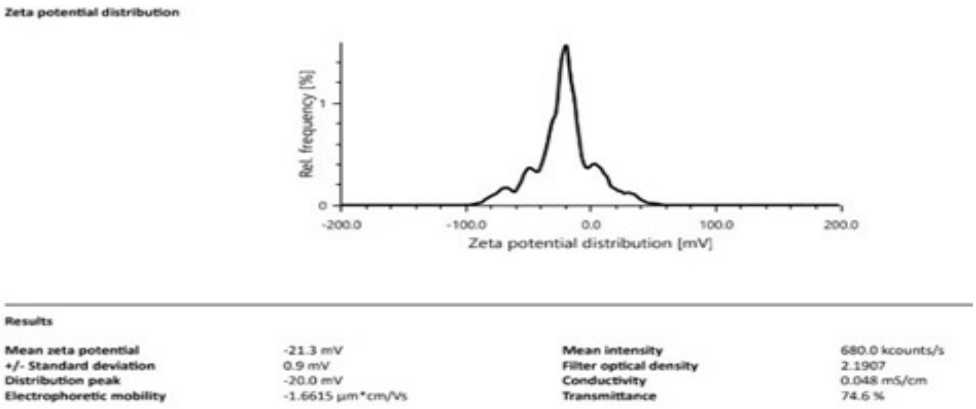

Figure 1 (e): Zeta potential of CuO nanoparticles

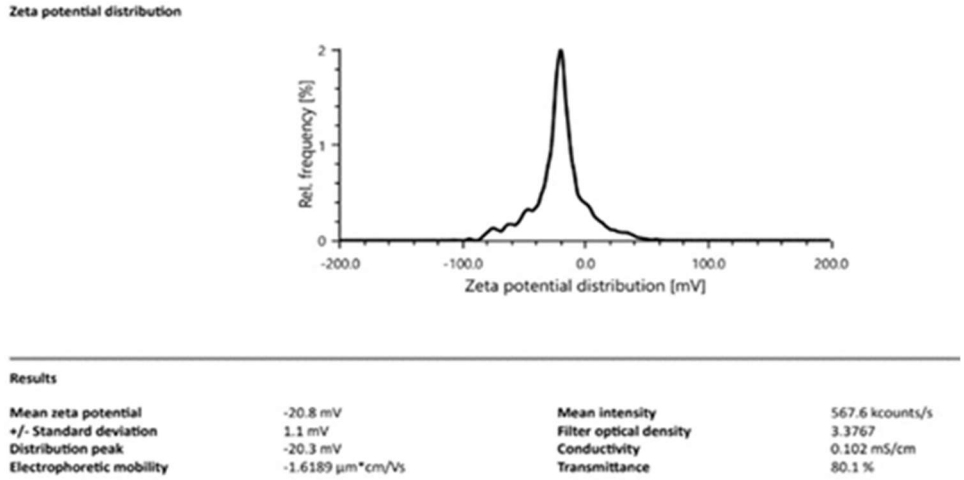

Figure 1 (f): Zeta potential of CuO nanoparticles

3.1.3 TGA

TGA provided insights into the thermal stability of CuO and ZnO nanoparticles. The TGA curve for CuO nanoparticles (Figure 2 (a)) showed an initial weight loss starting at approximately 78.3°C, with significant weight loss occurring around 213.7°C and the final weight loss phase at about 248.7°C. These temperature points reflect the thermal stability of CuO nanoparticles, with weight loss primarily due to the removal of residual moisture and adsorbed gases. In contrast, the TGA curve for ZnO nanoparticles, presented in the exact figure, indicated an initial weight loss beginning at approximately 65.4°C, a notable weight loss around 215.7°C, and a final significant weight loss observed at approximately 298.7°C. The higher final weight loss temperature for ZnO nanoparticles suggests the decomposition of surface-adsorbed organic components. Both nanoparticle types demonstrated good thermal stability, with their weight losses indicating minimal thermal degradation within the tested temperature range.

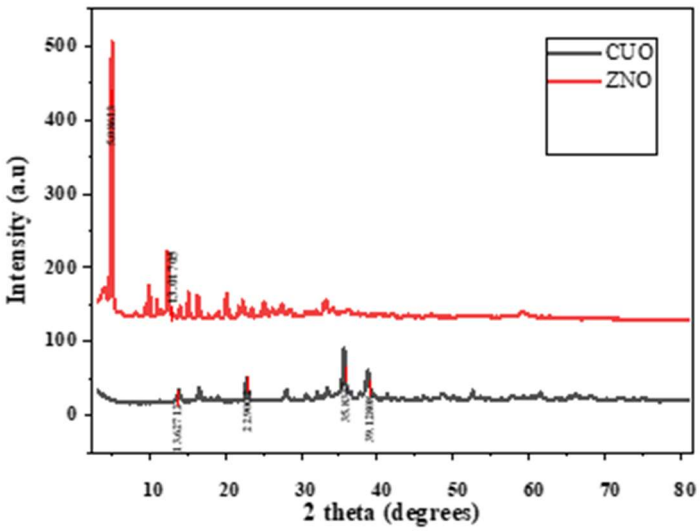

Figure 2 (a): TGA curves for CuO and ZnO

3.1.4 Powder XRD

Powder XRD analysis was performed to determine the crystalline structure of CuO and ZnO nanoparticles. The XRD pattern for CuO nanoparticles (Figure 2 (b)) showed peaks at 13.62°, 22.90°, 35.83°, and 39.12°. These relatively few broad peaks suggest that the CuO nanoparticles may exhibit some degree of amorphous character, indicating less crystalline order than more well-defined crystalline structures. In contrast, the XRD pattern for ZnO nanoparticles revealed prominent peaks at 5.08° and 13.01°, with other peaks appearing well-defined and sharp. This pattern indicates a high degree of crystallinity and confirms the hexagonal wurtzite structure of ZnO. The well-resolved peaks demonstrate that ZnO nanoparticles possess a more ordered crystalline structure than CuO nanoparticles. Overall, the XRD results highlight the differences in crystalline nature between CuO and ZnO nanoparticles.

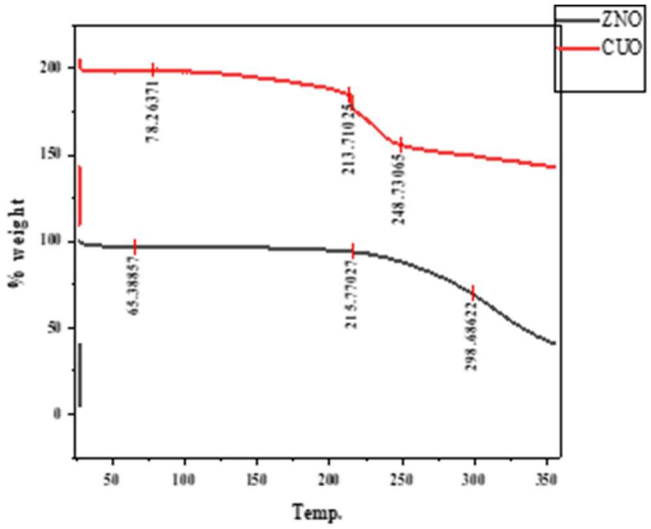

Figure 2 (b): XRD patterns for CuO and ZnO

3.2 Antioxidant activity

3.2.1 DPPH Radical Scavenging Activity

The DPPH radical scavenging activity was assessed to evaluate the antioxidant capacity of CuO and ZnO nanoparticles at various concentrations. CuO nanoparticles exhibited inhibition percentages of 12.0%, 18.0%, 31.5%, and 43.5% at 10, 20, 30, and 40 µg/mL concentrations, respectively. In contrast, at the same concentrations, ZnO nanoparticles showed higher inhibition percentages of 21.5%, 33.0%, 47.0%, and 57.0%. These results indicate that CuO nanoparticles possess more excellent antioxidant activity than ZnO nanoparticles, as evidenced by their lower inhibition percentages across all tested concentrations. (Table 1 (a)) represents the average absorbance values for the control and the samples and the calculated inhibition percentages for CuO and ZnO nanoparticles at different concentrations. (Figure 3 (a)) provides a graphical representation of the % scavenging activity versus concentration (µg/mL), highlighting the antioxidant activities of CuO and ZnO nanoparticles.

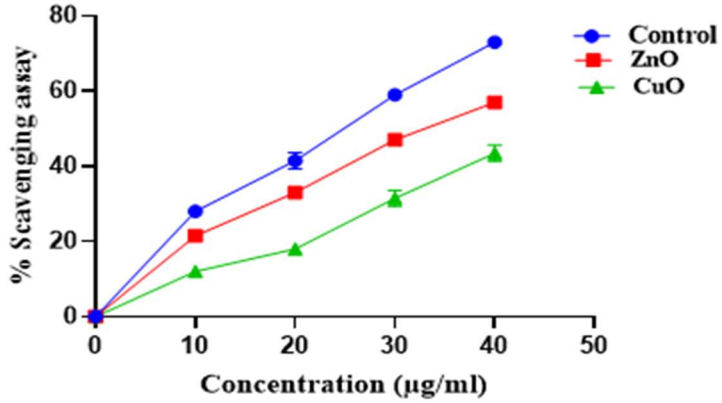

Figure 3 (a): Antioxidant activities of CuO and ZnO nanoparticles: (a) DPPH radical scavenging activity for CuO and ZnO nanoparticles

Table 1: Antioxidant activity of CuO and ZnO Nanoparticles

Table 1(a): DPPH Radical Scavenging Activity of CuO and ZnO Nanoparticles

Concentration (µg/mL)	Average Absorbance (Control)	Average Absorbance (CuO)	% Inhibiti (CuO)	Average Absorbance (ZnO)	% Inhibitio (ZnO)
10	0.700	0.616	12.0%	0.549	21.5%
20	0.700	0.574	18.0%	0.469	33.0%
30	0.700	0.479	31.5%	0.371	47.0%
40	0.700	0.396	43.5%	0.301	57.0%

3.2.2 ROS Scavenging Activity

The ROS scavenging activity of CuO and ZnO nanoparticles was evaluated at concentrations of 10, 20, 30, and 40 µg/mL. The results are summarised in (Table 1 (b)), with absorbance values for each concentration and corresponding percentage scavenging activity. CuO nanoparticles exhibited absorbance values of 0.504, 0.439, 0.317, and 0.261 at concentrations of 10, 20, 30, and 40 µg/mL, respectively, corresponding to scavenging percentages of 26.00%, 35.50%, 53.50%, and 61.50%. ZnO nanoparticles showed absorbance values of 0.534, 0.469, 0.406, and 0.344 at the same concentrations, with scavenging percentages of 21.50%, 31.00%, 40.50%, and 49.50%. (Figure 3 (b)) illustrates the % scavenging activity versus concentration for CuO and ZnO nanoparticles, demonstrating that CuO nanoparticles possess more excellent ROS scavenging activity than ZnO nanoparticles at all tested concentrations.

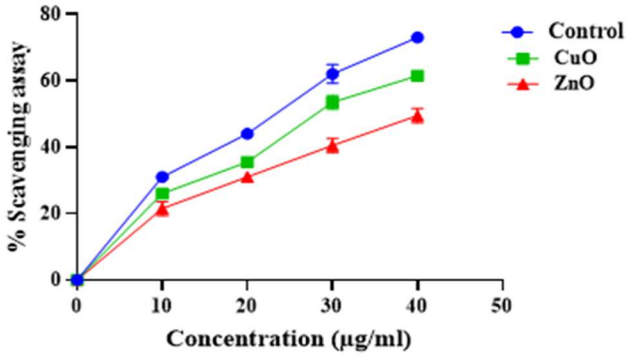

Figure 3 (b): RoS scavenging activity for CuO and ZnO nanoparticles

Table 1(b): ROS Scavenging Activity of CuO and ZnO Nanoparticles

Concentration (µg/mL)	Average Absorbance (Control)	Average Absorbance (CuO)	% Inhibition (CuO)	Average Absorbance (ZnO)	% Inhibition (ZnO)
10	0.680	0.504	26.00%	0.534	21.50%
20	0.680	0.439	35.50%	0.469	31.00%
30	0.680	0.317	53.50%	0.406	40.50%
40	0.680	0.261	61.50%	0.344	49.50%

3.3 Cytotoxicity assay

3.3.1 MTT assay

The cytotoxicity of CuO and ZnO nanoparticles was evaluated using the MTT assay with NIH 3T3 cells at 24 and 48 hours. At 24 hours, CuO nanoparticles exhibited average cell viability percentages of 100%, 95.26%, 93.00%, 84.70%, and 80.20% at 0, 10, 20, 30, and 40 µg/mL concentrations, respectively. In contrast, at the same concentrations, ZnO nanoparticles showed average viability percentages of 100%, 92.13%, 88.33%, 82.35%, and 78.99%. The results are illustrated in (Figure 4 (a)), which displays the cell viability at 24 hours. At 48 hours, CuO nanoparticles displayed average cell viability percentages of 100%, 96.30%, 92.15%, 88.50%, and 85.20%, while ZnO nanoparticles showed average viability percentages of 100%, 93.25%, 89.75%, 84.55%, and 81.10%. These results are depicted in (Table 2 and Figure 4 (b)), representing the cell viability at 48 hours. The data demonstrates that cell viability generally decreased with increasing nanoparticle concentration and incubation time, reflecting the cytotoxic effects of CuO and ZnO nanoparticles over time.

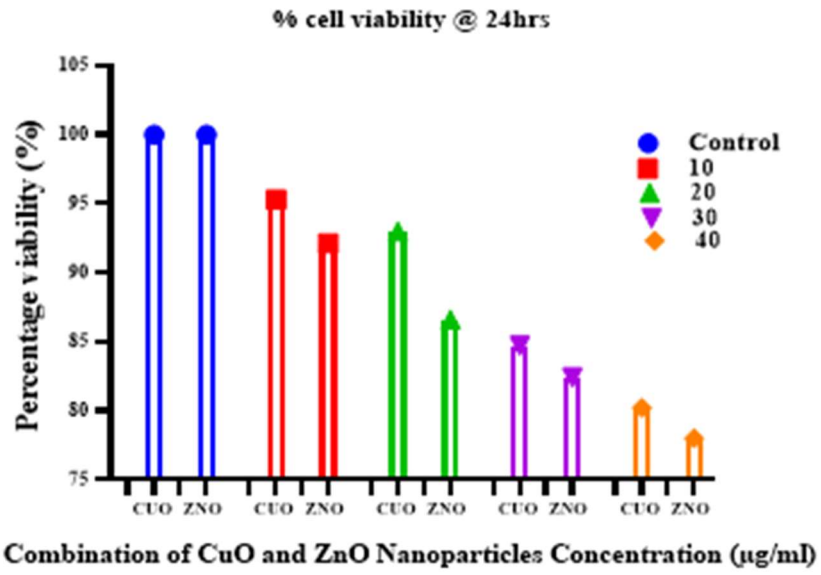

Figure 4 (a): MTT assay of Combination of CuO and ZnO nanoparticles concentration (ug/ml) @ 24 hrs

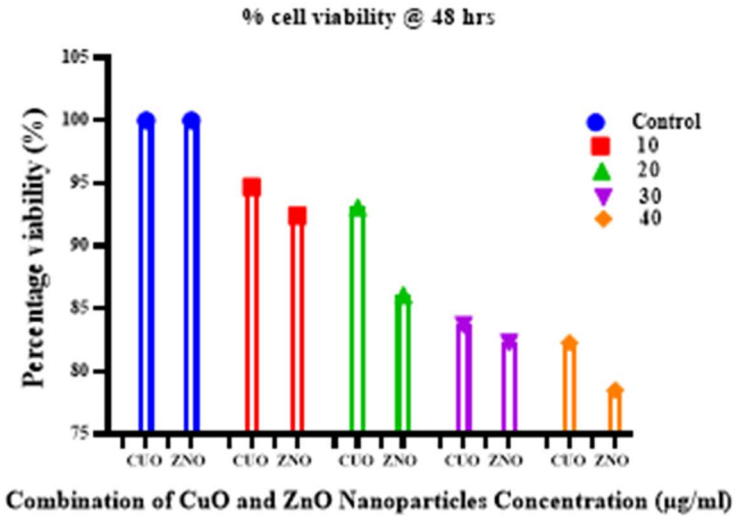

Figure 4 (b): MTT assay of Combination of CuO and ZnO nanoparticles concentration (ug/ml) @ 48 hrs

Table 2: Cell Viability of NIH 3T3 Cells Exposed to CuO and ZnO Nanoparticles at Various Concentrations for 24 and 48 hrs

Nanoparticle	Concentration (µg/mL)	Average Absorbance (24 Hours)	Average Absorbance (48 Hours)	Average Cell Viability (%) - 24 Hours	Average Cell Viability (%) - 48 Hours
Control	-	0.820	0.790	100	100
CUO	10	0.780	0.750	95.3	94.7
	20	0.770	0.740	93.0	93.1
	30	0.690	0.660	84.7	83.7
	40	0.660	0.650	80.2	82.3
ZNO	10	0.750	0.730	92.1	92.4
	20	0.710	0.680	86.6	86.1
	30	0.680	0.650	82.4	82.3
	40	0.650	0.620	78.0	78.5

3.3.2 Cell Proliferation Assay

The NIH 3T3 cells were treated with CuO and ZnO nanoparticles at concentrations of 10, 20, 30, and 40 µg/mL, and the percentage of cell proliferation was assessed after 24 and 48 hours. At 24 hours, CuO nanoparticles showed percentage cell proliferation of 90%, 85.7%, 80.9%, and 75.3% for concentrations of 10, 20, 30, and 40 µg/mL, respectively. At 48 hours, these values were 89.3%, 83.9%, 79.8%, and 74.5%. For ZnO nanoparticles, the percentage of cell proliferation at 24 hours was 85.7%, 78.6%, 72.5%, and 69.3%, and at 48 hours, the values were 83.4%, 76.7%, 70.8%, and 68.5% for the same concentrations. The control sample showed a consistent 100% cell proliferation at 24 and 48 hours. These results indicate that both CuO and ZnO nanoparticles impact cell proliferation in a dose-dependent manner, with higher concentrations leading to lower proliferation rates. The cell proliferation assay results for CuO and ZnO nanoparticles are presented in Table 3 and Figures 4 (c) and Figure 4 (d).

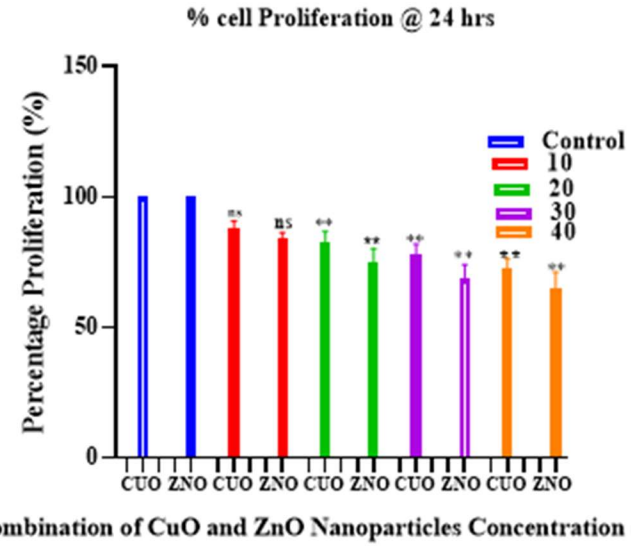

Figures 4 (c): % cell proliferation of Combination of CuO and ZnO nanoparticles concentration (ug/ml) @ 24 hrs

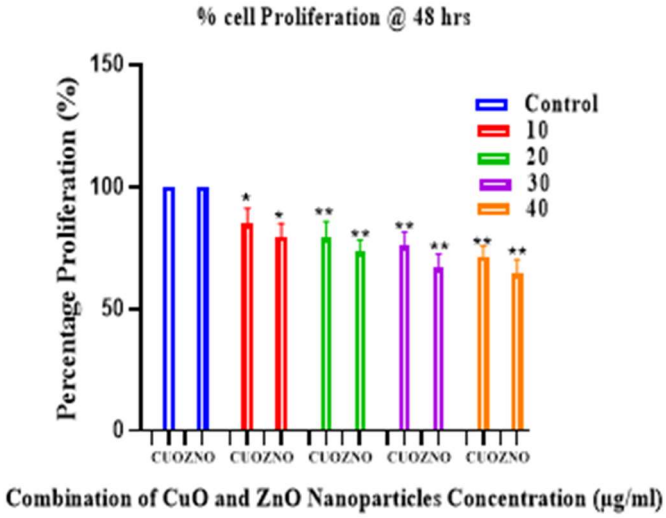

Figure 4 (d): % cell proliferation of Combination of CuO and ZnO nanoparticles concentration (ug/ml) @ 48 hrs

Table 3: Percentage of Cell Proliferation of NIH 3T3 Cells Exposed to CuO and ZnO Nanoparticles at Various Concentrations for 24 hrs and 48hrs

Nano particle	Concentration (µg/mL)	Average Absorbance (24 Hours)	Average Absorbance (48 Hours)	Average Cell Proliferation (%) - 24 Hours	Average Cell Viability (%) - 48 Hours
Control	-	0.850	0.820	100	100
CuO	10	0.765	0.733	90	89.3
	20	0.725	0.690	85.7	83.9
	30	0.685	0.660	80.9	79.8
	40	0.630	0.620	75.3	74.5
ZnO	10	0.727	0.683	85.7	83.4
	20	0.665	0.629	78.6	76.7
	30	0.615	0.581	72.5	70.8
	40	0.587	0.561	69.3	68.5

3.4 Wound scratch assay

The wound healing potential of CuO and ZnO nanoparticles was assessed using the scratch assay on NIH 3T3 cell lines, with measurements taken 24 hours post-treatment. CuO and ZnO nanoparticles were tested at 10, 20, 30, and 40 µg/mL concentrations. At 24 hours, CuO nanoparticles at 10 µg/mL showed 30% wound closure, increasing to 55%, 76%, and 90% at 20, 30, and 40 µg/mL concentrations, respectively. ZnO nanoparticles exhibited a similar trend, with 25% wound closure at 10 µg/mL and progressing to 50%, 70%, and 85% at 20, 30, and 40 µg/mL, respectively. These results indicate a concentration-dependent enhancement in wound healing for both CuO and ZnO nanoparticles at the 24-hour mark. CuO nanoparticles consistently showed slightly higher percentages of wound closure than ZnO nanoparticles at each concentration (figure 5 (a) and Figure 5 (b)). The data suggests that CuO nanoparticles may be more effective in promoting wound healing in NIH 3T3 cell lines, potentially offering a superior therapeutic benefit in wound management.

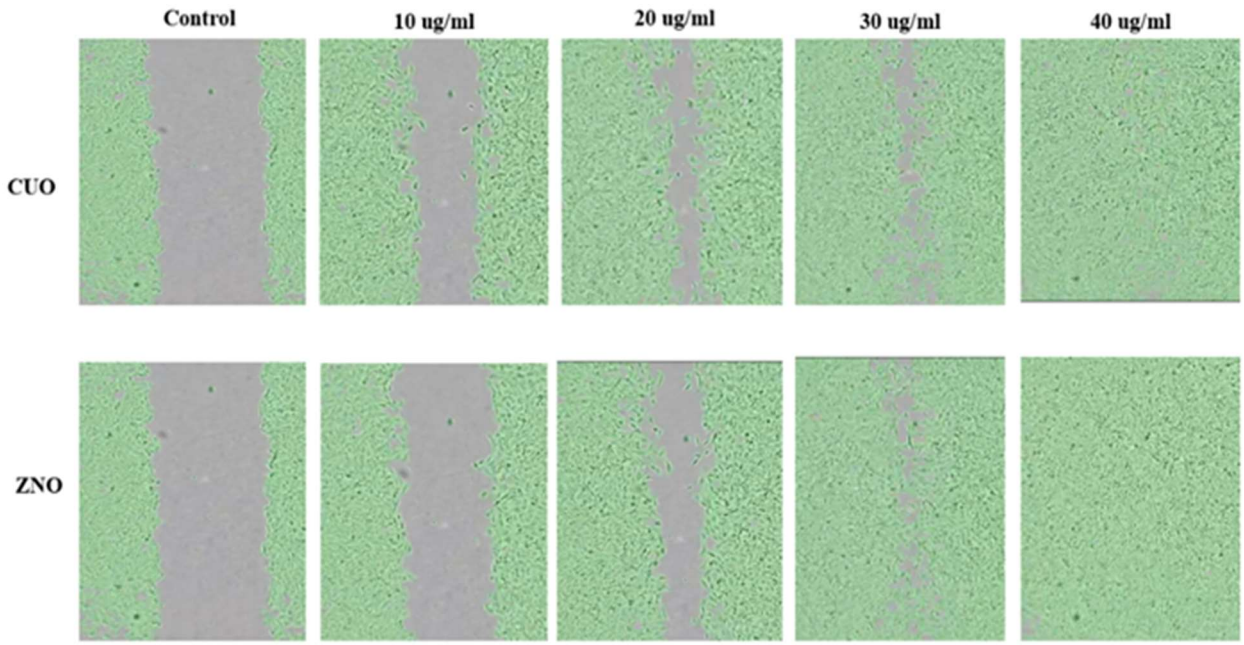

Figure 5 (a): Representative Images of Scratch Assay for CuO and ZnO Nanoparticles at 24 hours

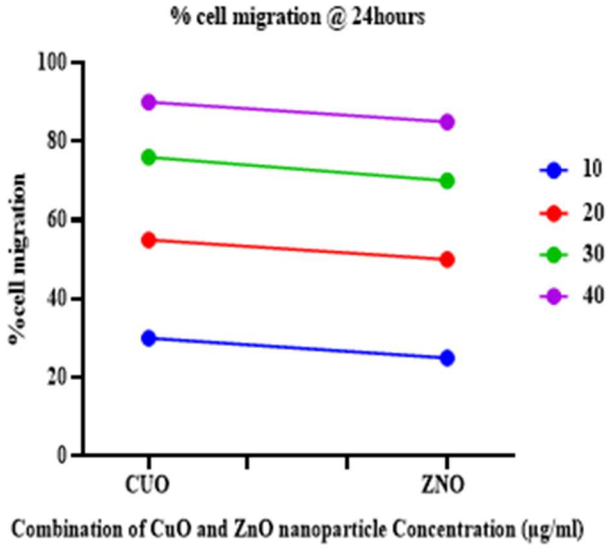

Figure 5 (b): Scratch Assay Results for Combination of CuO and ZnO Nanoparticles at 24 hours

3.5 Antibacterial study

The agar well diffusion method evaluated the antibacterial activity of CuO and ZnO nanoparticles against *E. coli* and *S. aureus*. Nanoparticles were tested at concentrations of 10, 20, 30, and 40 µg/mL, with the zones of inhibition measured after 24 hours of incubation. For E. coli, CuO nanoparticles exhibited zones of inhibition of 14 mm, 18 mm, 21 mm, and 26 mm at concentrations of 10, 20, 30, and 40 µg/mL, respectively (Figure 5 (c)). ZnO nanoparticles showed slightly smaller inhibition zones, measuring 12 mm, 15 mm, 18 mm, and 22 mm at the same respective concentrations. Against *S. aureus*, CuO nanoparticles produced zones of inhibition of 16 mm, 20 mm, 24 mm, and 30 mm at concentrations of 10, 20, 30, and 40 µg/mL, respectively (Figure 5 (d)). ZnO nanoparticles demonstrated smaller inhibition zones, with measurements of 14 mm, 18 mm, 22 mm, and 26 mm at the corresponding concentrations. These results, seen in Figure 5(e), indicate that CuO and ZnO nanoparticles possess significant antibacterial properties, with CuO nanoparticles consistently showing larger zones of inhibition against *E. coli* and *S. aureus* than ZnO nanoparticles.

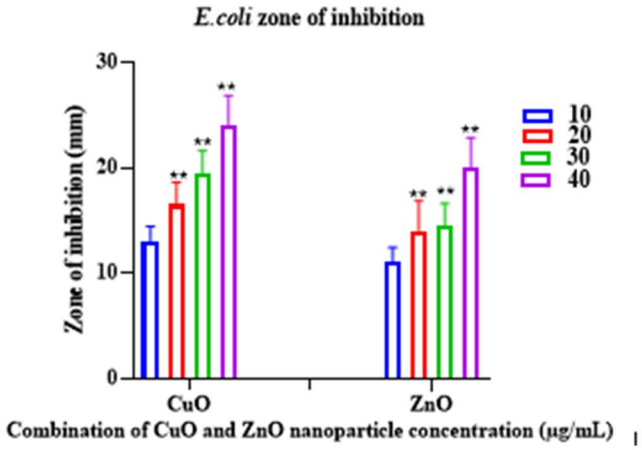

Figure 5 (c): Zones of Inhibition for E. coli Treated with Combination of CuO and ZnO Nanoparticles at Different Concentrations

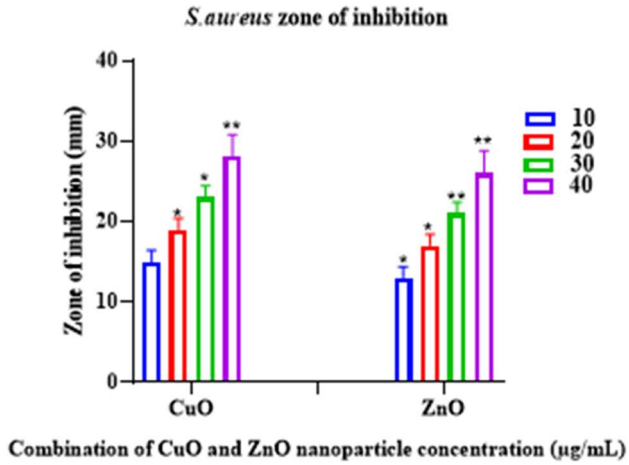

Figure 5 (d): Zones of Inhibition for S. aureus Treated with Combination of CuO and ZnO Nanoparticles at Different Concentrations

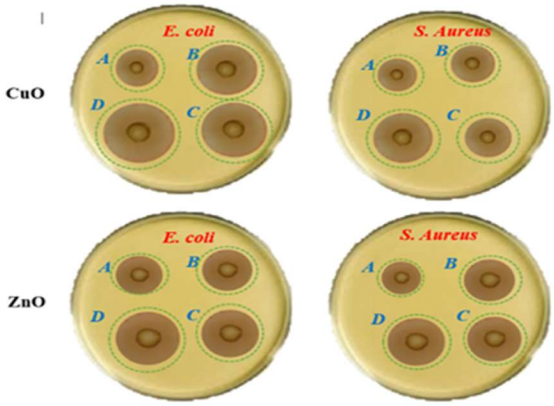

Figure 5 (e): Visual Representation of Antibacterial Activity of CuO and ZnO Nanoparticles Against E. coli and S. aureus.

3.6 Reduction in chronic inflammation

The concentrations of TNF-α and IL-10 in NIH 3T3 cells treated with CuO and ZnO nanoparticles were assessed at 24 hours and 48 hours using ELISA. The standard curves were plotted using absorbance values against known concentrations of TNF-α and IL-10, resulting in the equations y=0.0067x+0.1549 for TNF-α and y=0.0067x+0.1699 for IL-10 (Tables 4,5 &, 6). These equations were used to calculate the concentrations of TNF-α and IL-10 in the samples. The data revealed that TNF-α concentrations in cells treated with CuO nanoparticles ranged from 8.42 to 37.91 pg/mL at 24 hours and from 7.20 to 35.52 pg/mL at 48 hours, while ZnO nanoparticle treatment resulted in TNF-α concentrations ranging from 11.25 to 53.72 pg/mL at 24 hours and from 10.16 to 50.16 pg/mL at 48 hours (Figures 6 (c) and 6 (d)). For IL-10, CuO nanoparticle treatment resulted in concentrations ranging from 12.02 to 66.67 pg/mL at 24 hours and 11.11 to 63.88 pg/mL at 48 hours. In contrast, ZnO

nanoparticle treatment resulted in IL-10 concentrations ranging from 15.22 to 75.27 pg/mL at 24 hours and 14.37 to 71.76 pg/mL at 48 hours. These results indicate that both CuO and ZnO nanoparticles modulate the inflammatory response. ZnO nanoparticles show slightly higher concentrations of both TNF-α and IL-10 than CuO nanoparticles, suggesting a more pronounced inflammatory response modulation by ZnO nanoparticles.

Table 4: Concentrations of TNF-α in NIH 3T3 Cells Treated with CuO and ZnO Nanoparticles for 24 Hours and 48 Hours

Nanoparticle	Concentration (µg/mL)	TNF-α Concentration (24 Hours)	TNF-α Concentration (48 Hours)
CuO	10	8.42	7.20
	20	14.18	13.26
	30	25.82	24.09
	40	37.91	35.52
ZnO	10	11.25	10.16
	20	22.50	20.89
	30	41.34	38.43
	40	53.72	50.16

Table 5: Concentrations of IL-10 in NIH 3T3 Cells Treated with CuO and ZnO Nanoparticles for 24 Hours and 48 Hours

Nanoparticle	Concentration (µg/mL)	IL-10 Concentration (24 Hours)	IL-10 Concentration (48 Hours)
CuO	10	12.02	11.11
	20	18.90	17.46
	30	40.30	38.75
	40	66.67	63.88
ZnO	10	15.22	14.37
	20	27.31	25.76
	30	55.37	52.71
	40	75.27	71.76

Table 6: TNF-α and IL-10 Standard Curve Values

Concentration (µg/mL)	Absorbance	
	TNF-α	IL-10
0	0.154	0.169
10	0.221	0.236
20	0.288	0.303
30	0.355	0.370
40	0.421	0.4367

3.7 *In-vitro* drug release

The in vitro drug release profiles of CuO and ZnO nanoparticles at concentrations of 10, 20, 30, and 40 µg/mL revealed distinct release behaviors that fit the Higuchi model, indicating a diffusion-controlled release mechanism. CuO nanoparticles demonstrated an initial burst release within the first 6 hours, with approximately 10% released at 10 µg/mL within the first 2 hours and up to 55% by 72 hours. Higher concentrations exhibited similar release patterns, showing a rapid initial release followed by a sustained phase. ZnO nanoparticles also showed a burst release, with about 12% released at 10 µg/mL within the first 2 hours and up to 58% by 72 hours. The release profiles for both nanoparticles best fit the Higuchi model, indicating diffusion-controlled release mechanisms. ZnO nanoparticles exhibited a slightly higher cumulative release than CuO nanoparticles, suggesting that ZnO nanoparticles may offer a more effective release for applications requiring faster drug delivery. In contrast, CuO nanoparticles provide a sustained release profile. The detailed release profiles and kinetic model fits are illustrated in Tables 7 and 8, Figures 6 (e) and 6 (f).

Table 7: In Vitro Drug Release Profile of CuO Nanoparticles

Time (hours)	% Release at 10 µg/mL	% Release at 20 µg/mL	% Release at 30 µg/mL	% Release at 40 µg/mL
2	10	14	17	20
4	14	20	24	28
6	17	24	29	33
8	20	28	33	38

12	24	34	40	45
24	34	48	56	64
48	45	63	73	83
72	55	77	89	100

Table 8: In Vitro Drug Release Profile of ZnO Nanoparticles

Time (hours)	% Release at 10 µg/mL	% Release at 20 µg/mL	% Release at 30 µg/mL	% Release at 40 µg/mL
2	12	16	19	22
4	16	22	26	30
6	19	26	31	35
8	22	30	35	40
12	26	36	43	48
24	36	50	58	66
48	48	66	76	86
72	58	80	92	102

3.7.1 Release kinetics

The release kinetics of CuO and ZnO nanoparticles were evaluated to determine the best-fitting model for drug release behavior. The cumulative release data were plotted against the square root of time, and the resulting fits confirmed that both CuO and ZnO nanoparticles follow the Higuchi model, indicating a diffusion-controlled release mechanism. The regression equations and R^2 values for each concentration of CuO and ZnO nanoparticles are provided below. These results confirm that CuO and ZnO nanoparticles exhibit diffusion-controlled release profiles, fitting well with the Higuchi model. CuO nanoparticles showed a slight variance in the release rate across different concentrations, whereas ZnO nanoparticles demonstrated a more consistent release rate. These findings suggest that CuO nanoparticles provide a more sustained release profile, while ZnO nanoparticles might offer a quicker release for applications requiring faster drug delivery. The detailed release profiles and kinetic model fits are illustrated in Table 9.

Table 9: Higuchi Model Kinetics for CuO and ZnO Nanoparticles

Concentration (µg/mL)	Higuchi Model Equation		R^2 values	
	CuO	ZnO	CuO	ZnO
10	Y=6.429x+1.1398	Y=6.6909x+2.195	0.998	0.9967
20	Y=8.9936x+1.7767	Y=9.255x+2.832	0.9974	0.9966
30	Y=10.327x+2.854	Y=10.495x+4.804	0.9964	0.9375
40	Y=11.6x+3.8171	Y=11.777x+5.180	0.9954	0.9932

3.8 Angiogenesis (CAM assay)

The angiogenesis potential of CuO and ZnO nanoparticles was evaluated using the CAM assay. The assay was performed by treating the CAM with nanoparticle suspensions at concentrations of 10, 20, 30, and 40 µg/mL. After 72 hours of incubation, the CAMs were analyzed for new blood vessel formation. CuO nanoparticles demonstrated a significant increase in angiogenesis at all tested concentrations, with the highest angiogenic response observed at 40 µg/mL. Specifically, the number of new blood vessels formed increased proportionally with the concentration of CuO nanoparticles, indicating a dose-dependent angiogenic effect. At 10 µg/mL, an average of 28 new vessels were observed, increasing to 39 boats at 20 µg/mL, 52 vessels at 30 µg/mL, and peaking at 69 vessels at 40 µg/mL. ZnO nanoparticles also promoted angiogenesis, albeit to a lesser extent than CuO nanoparticles. The number of new blood vessels formed was 22 at 10 µg/mL, 32 at 20 µg/mL, 48 at 62 µg/mL, and 50 at 40 µg/mL. While ZnO nanoparticles exhibited a dose-dependent response, the overall angiogenic potential was slightly lower than CuO nanoparticles at the same concentrations. As seen in (Figures 6 (g) and 6 (h)). These results indicate that CuO and ZnO nanoparticles possess angiogenic properties, with CuO nanoparticles showing a more pronounced effect. The enhanced angiogenesis observed with CuO nanoparticles suggests their potential utility in promoting vascularization in wound healing applications, making them a promising candidate for further investigation in therapeutic angiogenesis.

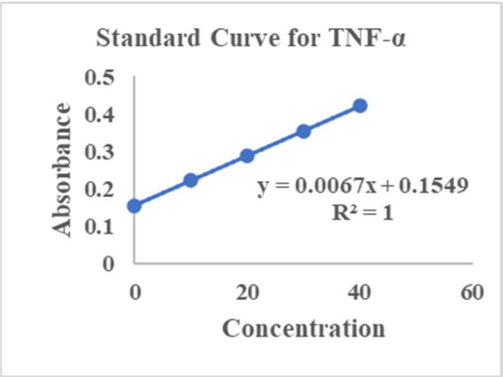

Figure 6 (a): Standard Curve for TNF-α

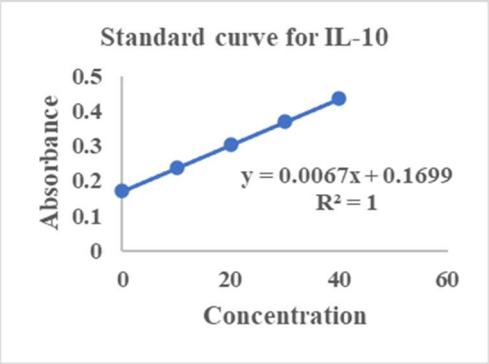

Figure 6 (b): Standard Curve for IL-10

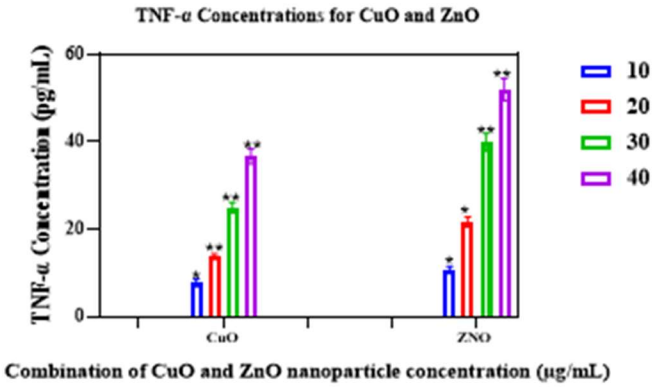

Figure 6 (c): Concentrations of TNF-α in NIH 3T3 Cells Treated with Combination of CuO and ZnO Nanoparticles for 24 Hours and 48 Hours

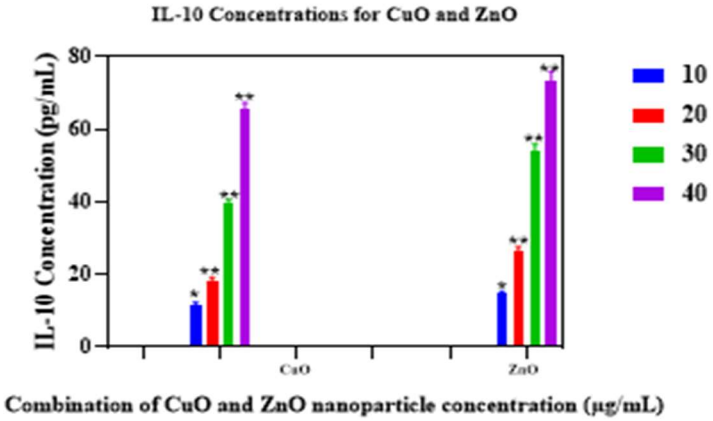

Figure 6 (d): Concentrations of IL-10 in NIH 3T3 Cells Treated with Combination of CuO and ZnO Nanoparticles for 24 Hours and 48 Hours

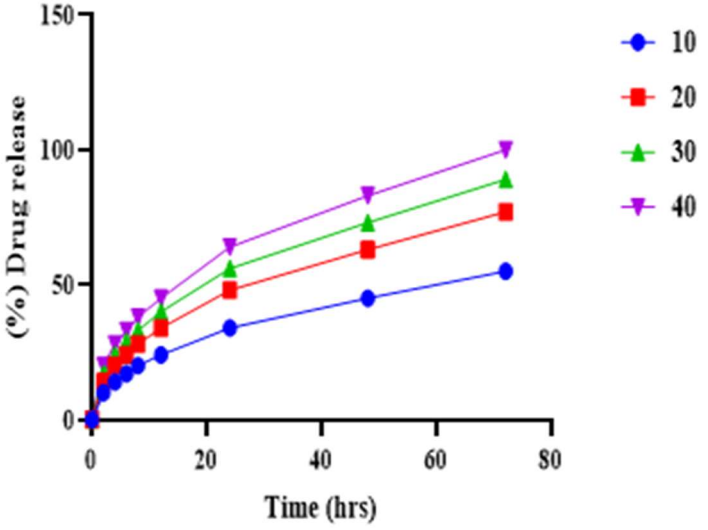

Figure 6 (e): In-Vitro Drug Release Profile of CuO Nanoparticles

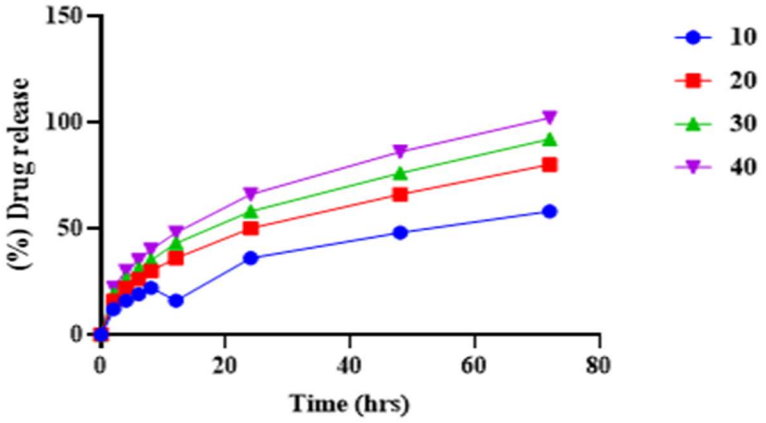

Figure 6 (f): In-Vitro Drug Release Profile of ZnO Nanoparticles

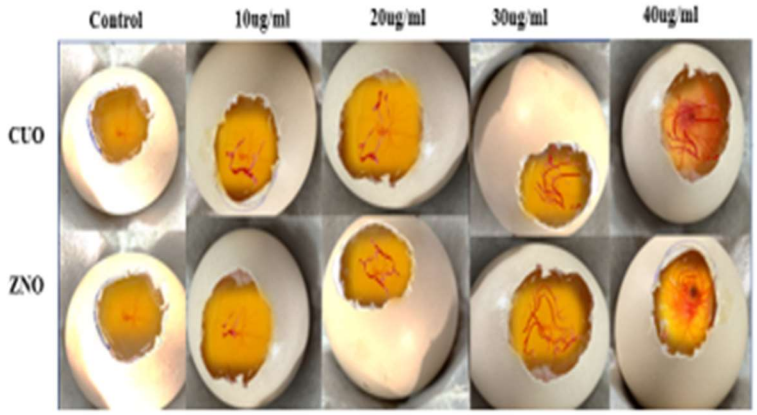

Figure 6 (g): Representative Images of Blood Vessel Formation in CAM Assay for CuO and ZnO Nanoparticles

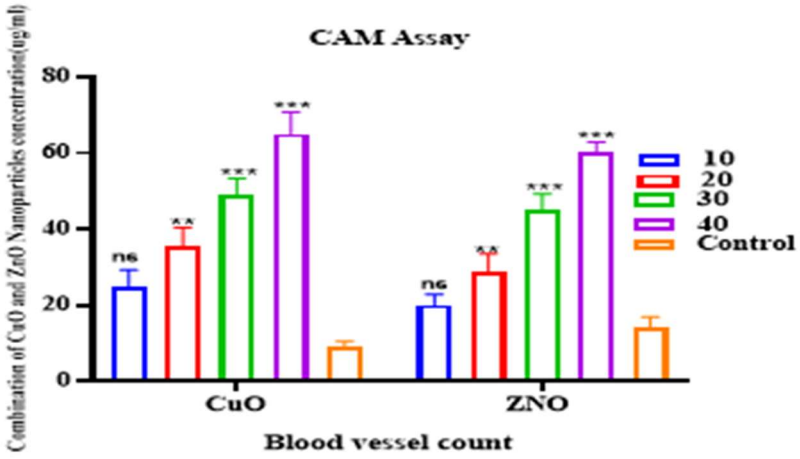

Figure 6 (h): Angiogenesis Potential of Combination of CuO and ZnO Nanoparticles Assessed by CAM Assay at Various Concentrations.

Discussion

Diabetic wounds pose a significant clinical challenge due to their chronic nature and high susceptibility to infections. This study explored the potential of CuO and ZnO nanoparticles in addressing the multifactorial issues associated with diabetic wound healing. We focused on their characterization, antibacterial properties, anti-inflammatory effects, and overall impact on wound healing processes.

Comprehensive characterization of CuO and ZnO nanoparticles was performed using XRD, SEM, and TGA techniques. The XRD analysis confirmed the crystalline nature of both nanoparticles, with CuO exhibiting peaks indicative of a monoclinic structure and ZnO showing a hexagonal wurtzite structure. These findings are consistent with the literature and ensure the purity and phase stability of the nanoparticles. SEM analysis revealed spherical and rod-shaped particles for CuO and ZnO, respectively, with uniform size distribution essential for predictable biological interactions. TGA demonstrated the thermal stability of the nanoparticles, which is a necessary consideration for their potential use in biomedical applications where thermal processes might be involved. These characterization studies are crucial as they ensure the reproducibility and reliability of the nanoparticles used in subsequent biological assays, thereby laying a solid foundation for their application in wound healing.

The antibacterial efficacy of CuO and ZnO nanoparticles was tested against *E. coli* and *S. aureus*. The results demonstrated that both types of nanoparticles possess significant antibacterial activity. CuO nanoparticles exhibited a larger zone of inhibition compared to ZnO nanoparticles, suggesting superior antibacterial properties. Specifically, CuO nanoparticles showed inhibition zones ranging from 14 mm to 26 mm for *E. coli* and 16 mm to 30 mm for *S. aureus*. ZnO nanoparticles exhibited inhibition zones ranging from 12 mm to 22 mm for *E. coli* and 14 mm to 26 mm for *S. aureus*. This enhanced antibacterial activity of CuO nanoparticles could be attributed to their ability to generate ROS, which

are known to damage bacterial cell walls and membranes. These findings are critical as they suggest that CuO nanoparticles might be more effective in reducing bacterial load at the wound site, thereby preventing infections and creating a conducive environment for wound healing.

The drug release profiles of CuO and ZnO nanoparticles were assessed at concentrations of 10, 20, 30, and 40 μg/mL. Both nanoparticles demonstrated an initial burst release within the first 6 hours, followed by a sustained release phase. For CuO nanoparticles, approximately 10% of the drug was released at 10 μg/mL within the first 2 hours, increasing to 55% by 72 hours. ZnO nanoparticles showed a similar pattern, with about 12% released at 10 μg/mL within the first 2 hours and up to 58% by 72 hours. The Higuchi model best described the release kinetics, indicating a diffusion-controlled mechanism. The slightly higher cumulative release observed for ZnO nanoparticles suggests they may offer more rapid drug delivery, whereas CuO nanoparticles provide a more sustained release profile. These release characteristics are crucial for tailoring therapeutic strategies to different stages of wound healing, where initial high drug concentrations might be needed to combat infection, followed by sustained release to promote tissue regeneration.

The anti-inflammatory properties of CuO and ZnO nanoparticles were evaluated by measuring pro-inflammatory cytokine TNF-α and anti-inflammatory cytokine IL-10 levels in treated NIH 3T3 cells. Both nanoparticles effectively modulated these cytokines, with ZnO nanoparticles showing slightly higher modulation. Specifically, CuO nanoparticle treatment resulted in TNF-α concentrations ranging from 8.42 to 37.91 pg/mL at 24 hours and 7.20 to 35.52 pg/mL at 48 hours, while ZnO nanoparticles resulted in TNF-α concentrations ranging from 11.25 to 53.72 pg/mL at 24 hours and 10.16 to 50.16 pg/mL at 48 hours. For IL-10, CuO nanoparticle treatment led to concentrations ranging from 12.02 to 66.67 pg/mL at 24 hours and 11.11 to 63.88 pg/mL at 48 hours, while ZnO nanoparticles resulted in IL-10 concentrations ranging from 15.22 to 75.27 pg/mL at 24 hours and 14.37 to 71.76 pg/mL at 48 hours. These results indicate that CuO and ZnO nanoparticles can modulate the inflammatory response. ZnO nanoparticles show a slightly more pronounced effect, suggesting their potential for reducing chronic inflammation in diabetic wounds. Additionally, the CAM assay assessed angiogenesis potential and revealed that both nanoparticles promoted blood vessel formation. CuO nanoparticles induced a higher degree of angiogenesis, as evidenced by the increased number of branching blood vessels, which is crucial for supplying nutrients and oxygen to the healing tissues.

The scratch assay results indicated that treatment with CuO and ZnO nanoparticles significantly enhanced cell migration in NIH 3T3 cells, a crucial process in wound healing. CuO nanoparticles demonstrated slightly better results, suggesting their potential to promote faster wound closure. Specifically, the cell migration rate was highest in the 40 μg/mL CuO group, with the wound gap closure reaching approximately 90% within 24 hours. ZnO nanoparticles also showed significant enhancement in cell migration, with the 40 μg/mL group achieving around 85% wound closure within the same period. These findings underscore the potential of these nanoparticles to accelerate wound healing by promoting cellular activities essential for tissue regeneration.

Conclusion

In conclusion, this study demonstrates the promising potential of CuO and ZnO nanoparticles in diabetic wound healing. Both nanoparticles exhibited significant antibacterial, anti-inflammatory, and pro-angiogenic properties, essential for effective wound management. CuO nanoparticles, in particular, showed a sustained release profile and superior antibacterial activity, making them a promising candidate for prolonged therapeutic applications. However, it is essential to note that metal oxides, while beneficial, can be hazardous if administered directly due to their potential to cause itching and discomfort at the wound site. Therefore, applying these nanoparticles in proper dosage forms is crucial to mitigate adverse effects and enhance their therapeutic impact. This study underscores the need for further research to optimize the dosage forms and validate CuO and ZnO nanoparticles' long-term safety and efficacy in clinical settings for diabetic wound healing.

Overall, the findings from this study highlight the multifaceted role of CuO and ZnO nanoparticles in addressing the complex pathology of diabetic wounds. Their ability to modulate inflammation, enhance antibacterial activity, promote angiogenesis, and support cell migration positions them as promising therapeutic agents for diabetic wound management. Future studies should focus on developing advanced delivery systems to ensure these nanoparticles have controlled and sustained release, minimising potential side effects and maximising their therapeutic benefits. This comprehensive evaluation lays the groundwork for future clinical applications of CuO and ZnO nanoparticles in chronic wound care, potentially transforming the treatment landscape for diabetic patients.

Abbreviations

CuO-Copper (II) Oxide

ZnO- Zinc Oxide

SEM- Scanning electron microscopy

XRD- Powder X-ray diffraction

TGA- Thermogravimetric Analysis

AGEs- Advanced glycation end-products

MMPs-Matrix Metalloproteinases

DLS-Dynamic Light Scattering

DMSO-Dimethyl Sulfoxide

ROS-Reactive Oxygen Species

H_2O_2-Hydrogen peroxide

DMEM-Dulbecco's Modified Eagle Medium

FBS-10% fetal bovine serum

PBS-Phosphate-buffered saline

CAM-Chick chorioallantoic membrane

Acknowledgments

The authors would like to thank the Department of Science and Technology - Fund for Improvement of Science and Technology Infrastructure (DST-FIST) and Promotion of University Research and Scientific Excellence (DST-PURSE) for the facilities provided for conducting the research.

Funding

The authors, Ms. Bogadi Subhasri, wish to express their gratitude to the Department of Science and Technology (DST-INSPIRE) Fellowship (ID IF200201) application reference no DST/INSPIRE/03/20 21/001920. New Delhi and technically approved by ICMR (Indian Council of Medical Research) with Fellowship ID 2021-8531.

References

Chen J, Qin S, Liu S, Zhong K, Jing Y, Wu X, Peng F, Li D, Peng C. Targeting matrix metalloproteases in diabetic wound healing. Frontiers in Immunology. 2023 Feb 17;14:1089001.

Huang C, Yuan W, Chen J, Wu LP, You T. Construction of smart biomaterials for promoting diabetic wound healing. Molecules. 2023 Jan 22;28(3):1110.

Van Putte L, De Schrijver S, Moortgat P. The effects of advanced glycation end products (AGEs) on dermal wound healing and scar formation: a systematic review. Scars, burns & healing. 2016 Nov 30;2:2059513116676828.

Nirenjen S, Narayanan J, Tamilanban T, Subramaniyan V, Chitra V, Fuloria NK, Wong LS, Ramachawolran G, Sekar M, Gupta G, Fuloria S. Exploring the contribution of pro-inflammatory cytokines to impaired wound healing in diabetes. Frontiers in immunology. 2023 Jul 27;14:1216321.

Zgutka K, Tkacz M, Tomasiak P, Tarnowski M. A role for advanced glycation end products in molecular ageing. International journal of molecular sciences. 2023 Jun 8;24(12):9881.

Bhardwaj H, Khute S, Sahu R, Jangde RK. Advanced drug delivery system for management of chronic diabetes wound healing. Current Drug Targets. 2023 Dec 1;24(16):1239-59.

Kolimi P, Narala S, Nyavanandi D, Youssef AA, Dudhipala N. Innovative treatment strategies to accelerate wound healing: trajectory and recent advancements. Cells. 2022 Aug 6;11(15):2439.

Oliveira A, Simões S, Ascenso A, Reis CP. Therapeutic advances in wound healing. Journal of Dermatological Treatment. 2022 Jan 2;33(1):2-2.
Burgess JL, Wyant WA, Abdo Abujamra B, Kirsner RS, Jozic I. Diabetic wound-healing science. Medicina. 2021 Oct 8;57(10):1072.
Singh KR, Nayak V, Singh J, Singh AK, Singh RP. Potentialities of bioinspired metal and metal oxide nanoparticles in biomedical sciences. RSC advances. 2021;11(40):24722-46.
Murali M, Kalegowda N, Gowtham HG, Ansari MA, Alomary MN, Alghamdi S, Shilpa N, Singh SB, Thriveni MC, Aiyaz M, Angaswamy N. Plant-mediated zinc oxide nanoparticles: advances in the new millennium towards understanding their therapeutic role in biomedical applications. Pharmaceutics. 2021 Oct 11;13(10):1662.
Panhwar S, Buledi JA, Mal D, Solangi AR, Balouch A, Hyder A. Importance and analytical perspective of green synthetic strategies of copper, zinc, and titanium oxide nanoparticles and their applications in pathogens and environmental remediation. Current Analytical Chemistry. 2021 Oct 1;17(8):1169-81.
Asif N, Amir M, Fatma T. Recent advances in the synthesis, characterization and biomedical applications of zinc oxide nanoparticles. Bioprocess and Biosystems Engineering. 2023 Oct;46(10):1377-98.
Prakashan D, Sahoo J, Gandhi S. Nanomaterial-Based Wound Therapy: Recent Advances and Future Perspectives. Nanomaterials for Biomedical and Bioengineering Applications. 2024 Apr 6:221-47.
Ehtesabi H, Fayaz M, Hosseini-Doabi F, Rezaei P. The application of green synthesis nanoparticles in wound healing: a review. Materials Today Sustainability. 2023 Mar 1;21:100272.
dos Santos Batista JG, Vigilato Rodrigues MÁ, de Freitas LF, Moreira Fonseca AC, de Souza Rodrigues A, Cunha da Cruz CP, Thipe VC, Lugão AB. Copper-Based Nanomaterials for Biologically Relevant Compounds. Copper-Based Nanomaterials in Organic Transformations. 2024:305-38.
Öztürk AB, Alarcin E, Yaşayan G, Avci-Adali M, Khosravi A, Zarepour A, Iravani S, Zarrabi A. Innovative approaches in skin therapy: bionanocomposites for skin tissue repair and regeneration. Materials Advances. 2024.
Govindasamy GA, SMN Mydin RB, Gadaime NK, Sreekantan S. Phytochemicals, biodegradation, cytocompatibility and wound healing profiles of chitosan film embedded green synthesized antibacterial ZnO/CuO nanocomposite. Journal of Polymers and the Environment. 2023 Oct;31(10):4393-409.
Aasy NK, El-Lakany SA, Masanga PM, Kamoun EA, El-Moslamy SH, Abu-Serie M, Aly RG, Elgindy NA. Concurrent tissue engineering for wound healing in diabetic rats utilizing dual actions of green synthesized CuO NPs prepared from two plants grown in Egypt. International Journal of Nanomedicine. 2023 Dec 31:1927-47.
Zheng Q, Chen C, Liu Y, Gao J, Li L, Yin C, Yuan X. Metal Nanoparticles: Advanced and Promising Technology in Diabetic Wound Therapy. International Journal of Nanomedicine. 2024 Dec 31:965-92.

Asif N, Amir M, Fatma T. Recent advances in the synthesis, characterization and biomedical applications of zinc oxide nanoparticles. Bioprocess and Biosystems Engineering. 2023 Oct;46(10):1377-98.
Zheng Q, Chen C, Liu Y, Gao J, Li L, Yin C, Yuan X. Metal Nanoparticles: Advanced and Promising Technology in Diabetic Wound Therapy. International Journal of Nanomedicine. 2024 Dec 31:965-92.
Kumari N, Sudharsan V, Kutty TM, Jayan N, Bhatlu ML. Green synthesis and characterization of Zinc and Copper oxides nanocomposite using Phyllanthus emblica extracts and its antibacterial and antioxidant properties. Materials Today: Proceedings. 2023 Jul 1.
Gaber SE, Hashem AH, El-Sayyad GS, Attia MS. Antifungal activity of myco-synthesized bimetallic ZnO-CuO nanoparticles against fungal plant pathogen Fusarium oxysporum. Biomass Conversion and Biorefinery. 2023 Jul 20:1-5.
Khoshsang H, Abbasi K, Ghaffarinejad A. Biosynthesis of ZnO and CuO nanoparticles using sunflower petal extract. Inorganic Chemistry Communications. 2023 Sep 1;155:111083.
Morales-Mendoza JE, Herrera-Pérez G, Fuentes-Cobas L, Hermida-Montero LA, Pariona N, Paraguay-Delgado F. Synthesis, structural and optical properties of Cu doped ZnO and CuO–ZnO composite nanoparticles. Nano-Structures & Nano-Objects. 2023 Apr 1;34:100967.
Mohamed M, Jayiz M, Alshammari AS, Sedky A, Khan ZR. Comparative study on structural, morphological, optical and photocatalytic properties of Mn3O4/ZnO, CuO/ZnO and Fe2O3/ZnO nanocomposites. Optical and Quantum Electronics. 2023 Jun;55(6):562.
Abebe B, Tsegaye D, Sori C, Renuka Prasad RC, Murthy HA. Cu/CuO-doped ZnO nanocomposites via solution combustion synthesis for catalytic 4-nitrophenol reduction. ACS omega. 2023 Mar 2;8(10):9597-606.
Iqbal A, ul Haq A, Rios-Aspajo L, Iturriaga-Chavez A. Bio-inspired synthesis of CuO and ZnO nanoparticles by hydrothermal method: characterization and evaluation as photocatalytic degradation of imidacloprid pesticide. GLOBAL NEST JOURNAL. 2023 Nov 1;25(9):150-8.
Morales-Mendoza JE, Herrera-Pérez G, Fuentes-Cobas L, Hermida-Montero LA, Pariona N, Paraguay-Delgado F. Synthesis, structural and optical properties of Cu doped ZnO and CuO–ZnO composite nanoparticles. Nano-Structures & Nano-Objects. 2023 Apr 1;34:100967.
Jeevarathinam M, Asharani IV. Synthesis of CuO, ZnO nanoparticles, and CuO-ZnO nanocomposite for enhanced photocatalytic degradation of Rhodamine B: a comparative study. Scientific Reports. 2024 Apr 27;14(1):9718.
Nguyen TT, Nguyen YN, Tran XT, Nguyen TT, Van Tran T. Green synthesis of CuO, ZnO and CuO/ZnO nanoparticles using Annona glabra leaf extract for antioxidant, antibacterial and photocatalytic activities. Journal of Environmental Chemical Engineering. 2023 Oct 1;11(5):111003.
Kumar R, Kumar K, Thakur N. Biosynthesis of CuO/Cu2O-ZnO nanocomposites via Commelina benghalensis leaf extract and their antibacterial, photocatalytic and antioxidant assessment. Inorganic Chemistry Communications. 2023 Nov 1;157:111400.

Madeshwaran K, Venkatachalam R. Green synthesis of bimetallic ZnO–CuO nanoparticles using Annona muricata l. extract: Investigation of antimicrobial, antioxidant, and anticancer properties. Journal of Industrial and Engineering Chemistry. 2024 Jun 6.
Nguyen TT, Nguyen YN, Tran XT, Nguyen TT, Van Tran T. Green synthesis of CuO, ZnO and CuO/ZnO nanoparticles using Annona glabra leaf extract for antioxidant, antibacterial and photocatalytic activities. Journal of Environmental Chemical Engineering. 2023 Oct 1;11(5):111003.
Rehman RU, Khan B, Aziz T, Gul FZ, Nasreen S, Zia M. Postponement growth and antioxidative response of Brassica nigra on CuO and ZnO nanoparticles exposure under soil conditions. IET nanobiotechnology. 2020 Jul;14(5):423-7.
Dzhambazov B, Batsalova T, Merky P, Lange F, Holmdahl R. NIH/3T3 Fibroblasts Selectively Activate T Cells Specific for Posttranslationally Modified Collagen Type II. International Journal of Molecular Sciences. 2023 Jun 28;24(13):10811.
Rahimi AM, Cai M, Hoyer-Fender S. Heterogeneity of the NIH3T3 fibroblast cell line. Cells. 2022 Aug 28;11(17):2677.
Jabeen A, Khan A, Ahmad P, Khalid A, Majeed Z, Anjum Z, Modafer Y, Jefri OA, Alanazi AM, Saeedi AM, Alsehli AH. Biomedical and photocatalytic dye degradation studies of Cymbopogon citratus mediated copper oxide nanoparticles (CuO NPs). Journal of Drug Delivery Science and Technology. 2023 Sep 1;87:104795.
Xie J, Li H, Zhang T, Song B, Wang X, Gu Z. Recent advances in ZnO nanomaterial-mediated biological applications and action mechanisms. Nanomaterials. 2023 Apr 27;13(9):1500.
Sandra S, Anakha DR, Silpa C, Vyshnavi TV, Bhagiyalakshmi M, Yamuna R, Karthega M. Synthesis of electrospun PVA/chitosan nanofibrous scaffold impregnated with CuO nanoparticles for wound healing. Cellulose. 2024 May 31:1-5.
Xie J, Li H, Zhang T, Song B, Wang X, Gu Z. Recent advances in ZnO nanomaterial-mediated biological applications and action mechanisms. Nanomaterials. 2023 Apr 27;13(9):1500.
Pérez-Díaz MA, Prado-Prone G, Díaz-Ballesteros A, González-Torres M, Silva-Bermudez P, Sánchez-Sánchez R. Nanoparticle and nanomaterial involvement during the wound healing process: an update in the field. Journal of Nanoparticle Research. 2023 Feb;25(2):27.
Sandra S, Anakha DR, Silpa C, Vyshnavi TV, Bhagiyalakshmi M, Yamuna R, Karthega M. Synthesis of electrospun PVA/chitosan nanofibrous scaffold impregnated with CuO nanoparticles for wound healing. Cellulose. 2024 May 31:1-5.
Sheikh-Oleslami S, Tao B, D'Souza J, Butt F, Suntharalingam H, Rempel L, Amiri N. A Review of Metal Nanoparticles Embedded in Hydrogel Scaffolds for Wound Healing In Vivo. Gels 2023, 9, 591.
Nguyen TT, Nguyen YN, Tran XT, Nguyen TT, Van Tran T. Green synthesis of CuO, ZnO and CuO/ZnO nanoparticles using Annona glabra leaf extract for antioxidant, antibacterial and photocatalytic activities. Journal of Environmental Chemical Engineering. 2023 Oct 1;11(5):111003.
Aasy NK, El-Lakany SA, Masanga PM, Kamoun EA, El-Moslamy SH, Abu-Serie M, Aly RG, Elgindy NA. Concurrent tissue engineering for wound healing in diabetic rats utilizing dual actions of green synthesized CuO NPs prepared from two plants grown in Egypt. International Journal of Nanomedicine. 2023 Dec 31:1927-47.

Worku LA, Nigussie Y, Bachheti A, Bachheti RK, Husen A. Antimicrobial activities of nanomaterials. InAdvances in smart nanomaterials and their applications 2023 Jan 1 (pp. 127-148). Elsevier.
Loera-Valencia R, Neira RE, Urbina BP, Camacho A, Galindo RB. Evaluation of the therapeutic efficacy of dressings with ZnO nanoparticles in the treatment of diabetic foot ulcers. Biomedicine & Pharmacotherapy. 2022 Nov 1;155:113708.
Lo S, Mahmoudi E, Fauzi MB. Applications of drug delivery systems, organic, and inorganic nanomaterials in wound healing. Discover Nano. 2023 Aug 22;18(1):104.
Prakashan D, Roberts A, Gandhi S. Recent advancement of nanotherapeutics in accelerating chronic wound healing process for surgical wounds and diabetic ulcers. Biotechnology and Genetic Engineering Reviews. 2023 Jan 17:1-29.
Lofty MJ. Elucidating the intracellular signalling pathways that mediate nanomaterial induced pro-inflammatory cytokine production in pulmonary cells in vitro (Doctoral dissertation, Heriot-Watt University).
Mahamuni-Badiger P, Dhanavade MJ. Challenges and toxicity assessment of inorganic nanomaterials in biomedical applications: Current status and future roadmaps. Journal of Drug Delivery Science and Technology. 2023 Aug 1:104806.
Wang Y, Feng Y, Yan J, Han X, Song P, Wu Y, Wang X, Mu Z, Li X, Zhang H. Spiky surface topography of heterostructured nanoparticles for programmable acceleration of multistage wound healing. Materials Today Nano. 2023 Aug 1;23:100351.
Mao Y, Sun Y, Yang C. Compound Microalgae-Type Biofunctional Hydrogel for Wound Repair during Full-Thickness Skin Injuries. Polymers. 2024 Mar 3;16(5):692.
Pérez-Díaz MA, Prado-Prone G, Díaz-Ballesteros A, González-Torres M, Silva-Bermudez P, Sánchez-Sánchez R. Nanoparticle and nanomaterial involvement during the wound healing process: an update in the field. Journal of Nanoparticle Research. 2023 Feb;25(2):27.
Huang F, Lu X, Yang Y, Yang Y, Li Y, Kuai L, Li B, Dong H, Shi J. Microenvironment-based diabetic foot ulcer nanomedicine. Advanced Science. 2023 Jan;10(2):2203308.
Gaddigal AT, Shivappa P, Ganeshkar MP, Mirjankar MR, Poojari PB, Huyilagola PV, Irannanavar KM, Goder PH, Kamanavalli CM. Green synthesis of copper oxide nanoparticles using Simarouba glauca leaf extract, characterization and screening for their biological applications. Journal of Dispersion Science and Technology. 2024 May 6:1-5.